Water and an Escaping Helium Tail Detected in the Hazy and Methane-depleted Atmosphere of HAT-P-18b from JWST NIRISS/SOSS

Guangwei Fu[1] , Néstor Espinoza[2] , David K. Sing[3,4] , Joshua D. Lothringer[5] , Leonardo A. Dos Santos[2] ,
Zafar Rustamkulov[4] , Drake Deming[6] , Eliza M.-R. Kempton[6] , Thaddeus D. Komacek[6] , Heather A. Knutson[7] ,
Loïc Albert[8] , Klaus Pontoppidan[2] , Kevin Volk[2], and Joseph Filippazzo[2]

[1] Department of Physics and Astronomy, Johns Hopkins University, Baltimore, MD 21218, USA; guangweifu@gmail.com
[2] Space Telescope Science Institute, 3700 San Martin Drive, Baltimore, MD 21218, USA
[3] Department of Physics and Astronomy, Johns Hopkins University, Baltimore, MD 21218, USA
[4] Department of Earth & Planetary Sciences, Johns Hopkins University, Baltimore, MD 21218, USA
[5] Department of Physics, Utah Valley University, Orem, UT 84058, USA
[6] Department of Astronomy, University of Maryland, College Park, MD 20742, USA
[7] Division of Geological and Planetary Sciences, California Institute of Technology, 1200 East California Boulevard, Pasadena, CA 91125, USA
[8] Institut de Recherche sur les Exoplanètes (iREx), Université de Montréal, Département de Physique, C.P. 6128 Succ. Centre-ville, Montréal, QC H3C 3J7, Canada

Abstract

JWST is here. The early release observation (ERO) program provides us with the first look at the scientific data and the spectral capabilities. One of the targets from the ERO is HAT-P-18b, an inflated Saturn-mass planet with an equilibrium temperature of ∼850 K. We present the NIRISS/SOSS transmission spectrum of HAT-P-18b from 0.6 to 2.8 μm and reveal the planet in the infrared beyond 1.6 μm for the first time. From the spectrum, we see clear water and escaping helium tail features in an otherwise very hazy atmosphere. Our free chemistry retrievals with ATMO show moderate Bayesian evidence (3.79) supporting the presence of methane, but the spectrum does not display any clearly identifiable methane absorption features. The retrieved methane abundance is ∼2 orders of magnitude lower than that of solar composition. The methane-depleted atmosphere strongly rejects simple equilibrium chemistry forward models with solar metallicity and a C/O ratio and disfavors high metallicity (100 times) and a low C/O ratio (0.3). This calls for additional physical processes such as vertical mixing and photochemistry, which can remove methane from the atmosphere.

Unified Astronomy Thesaurus concepts: Exoplanet atmospheres (487); Exoplanet atmospheric composition (2021); Exoplanet astronomy (486)

Supporting material: machine-readable table

1. Introduction

The era of JWST has finally arrived (The JWST Transiting Exoplanet Community Early Release Science Team et al. 2022). The unparalleled infrared capability and photometric precision from JWST will evermore change our understanding of exoplanet atmospheres. With the expanded spectral windows into the infrared, we can now identify and measure new molecular features that have never been studied in detail before. Methane, an abundant chemical species on Earth and many solar system planets, has yet to be detected in a short-period exoplanet atmosphere. It is one of the most significant byproducts of life activities on Earth, and detecting methane is one of the many required steps to eventually finding evidence of carbon-based life as we know it beyond Earth.

Methane is ample in solar system gas giants (Jupiter, Saturn, Uranus, and Neptune) where the upper atmosphere is cooler than 200 K. The lack of evidence for methane in short-period exoplanet atmospheres has been puzzling (Stevenson et al. 2010; Kreidberg et al. 2019) as equilibrium chemistry forward models predict the rise of the methane abundance in sub-1000 K exoplanet atmospheres (Moses et al. 2011; Benneke et al. 2019). Methane can be destroyed at high temperatures

(Zahnle & Marley 2014) and it also has a short photochemical lifetime (Kasting et al. 1983; Miller-Ricci Kempton et al. 2012; Thompson et al. 2022). Measurements of methane abundances in exoplanet atmospheres will help us to better understand atmospheric vertical mixing based on interior thermal structure and photochemistry (Fortney et al. 2020).

HAT-P-18b is a Saturn-like planet with a mass of 0.197 $M_{\rm Jup}$ and a radius of 0.995 $R_{\rm Jup}$ (Hartman et al. 2012). It has an equilibrium temperature of ∼850 K. The relatively low temperature compared to other hot Jupiters (>1000 K) makes it an intriguing target for atmospheric characterization to study disequilibrium chemistry (Fortney et al. 2020), especially its impacts on methane abundance (Zahnle & Marley 2014; Tsai et al. 2021).

Here we present the transmission spectrum of HAT-P-18b obtained using JWST Near Infrared Imager and Slitless Spectrograph single object slitless spectroscopy (NIRISS/SOSS), which covers ∼0.6 to 2.8 μm. Our data are sensitive to multiple molecular features from water and methane, which should allow us to robustly detect and measure their abundance. The long continuous wavelength coverage extending into the optical also allows us to place tight constraints on HAT-P-18b's aerosol properties. In this Letter, we report the clear detection of water, an escaping helium tail, a sub-Rayleigh haze scattering slope, and methane depletion in the atmosphere of HAT-P-18b.
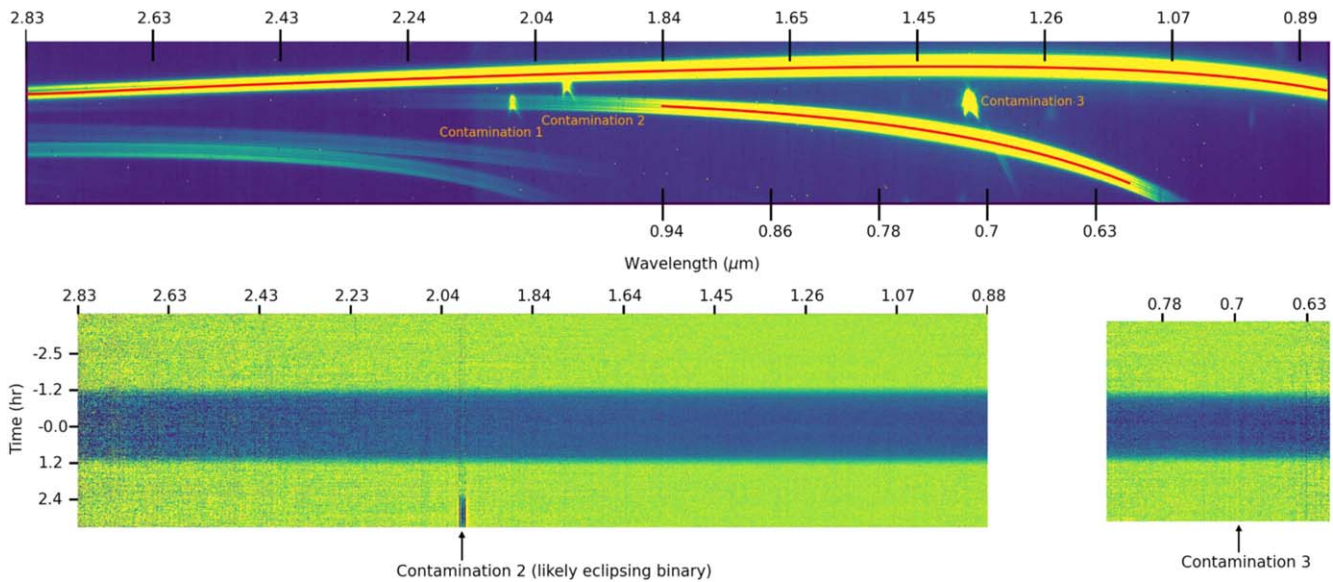
Figure 1. The top panel shows one of the integrations from `rateints.fits` files; the red lines show the first- and second-order spectra traces. The wavelength-dependent zodiacal light background and three zeroth-order nearby contamination stars are visible in the image. The bottom panel shows the reduced light curve at every pixel bin. Contamination 1 has a minimal effect on the planet spectrum as it is far away from the first order and not extracted in the second order. We detect a time-varying flux level in contamination 2 (~12% dimming), which is likely caused by an eclipsing binary. Contamination 3 has a spike going across the second-order spectrum, which leads to wavelength-dependent dilution effects. We removed the contaminated parts of the spectrum from sources two and three in the analysis.

2. Observations and Data Reduction

This data set was collected as part of the early release observation program (program ID: 2734; Pontoppidan et al. 2022). A transit of HAT-P-18b was observed using NIRISS/SOSS on 2022 June 13 with the GR700XD grism and the CLEAR filter. The SUBSTRIP256 detector was used to capture both order one and order two of the dispersed spectra. A total of 7.15 hr of time series observation was taken to ensure sufficient out-of-transit baseline coverage. There are nine groups per integration with each integration taking 54.94 s and a total of 469 integrations.

2.1. Data Reduction

We begin our data reduction with the `rateints.fits` data downloaded from the MAST archive on 2022 July 28. The products are generated from the JWST Science Calibration Pipeline stage 2a, which fits the accumulating signal ramp for every pixel in each integration. One integration of the `rateints.fits` file is shown in the top panel of Figure 1. The image from the SUBSTRIP256 subarray has a dimension of 2048 × 256 pixels with a wavelength increasing from right to left. Since SOSS mode is slitless, contamination from nearby stars and the sky background can dilute transit signals. The first step is to remove the zodiacal light background, which increases with wavelength with a sharp drop around 2.1 μm caused by the edges of the pick-off mirror. We used the smoothed background template from the commissioning observation (observation 5 of program 1541) downloaded from `jwst-docs`.[9] The background template is first scaled based on the median of the bottom 20 percentile pixels between columns 300 and 500 (~2.3 to 2.5 μm) and then subtracted from every integration. Since we do not expect the zodiacal light background to be time-dependent on our 7.15 hr timescale, we subtract the same scaled background template from all integrations.

Next, we determine the first- and second-order spectral trace locations by first taking the point-spread function from the bright first-order spectral region (~1.5 μm) and then cross correlating it at every column. The peak cross-correlation values at each column as a function of column pixel values are then fitted with a polynomial to smooth out the effects of contamination and bright outlier pixels. The first-order spectrum is then extracted with a width of 60 pixels centered at the trace as shown in red lines in the upper panel of Figure 1. The `scipy.interpolate.interp1d` function is used at each column to interpolate each extraction at the subpixel levels. The same steps are then used to extract the second-order spectra after the first order is extracted from the 2D image.

After the first- and second-order spectra have been extracted and aligned in the y-axis, we applied a median filter along each row to remove all outlier bright pixels within the 60 pixel wide spectral cut. Then we subtract the median of the combined top and bottom 15 pixels at each 60 pixel wide column to remove the $1/f$ noise. At last, we sum the middle 30 pixels at each extracted spectral column for every integration to get the light curves for all wavelength channels. All the cleaned light curves at each column are shown in the lower panel of Figure 1.

2.2. Light-curve Fitting

We first fit the white light data using the `Batman` (Kreidberg 2015) transiting light-curve model with `emcee` (Foreman-Mackey et al. 2013). There are a total of six free parameters in the fit including the midtransit time, transit depth, semimajor axis, inclination, linear slope, and a constant offset. There is a starspot crossing event during the transit that changes the transit light-curve shape in a wavelength-dependent way (left panel of Figure 2). We mask out the starspot crossing (integration 240 to 272) during the white light fit. After subtracting the best-fit model, we fit a polynomial model to the starspot crossing residual. Since the starspot shape varies as a function of wavelength due to its different temperature relative
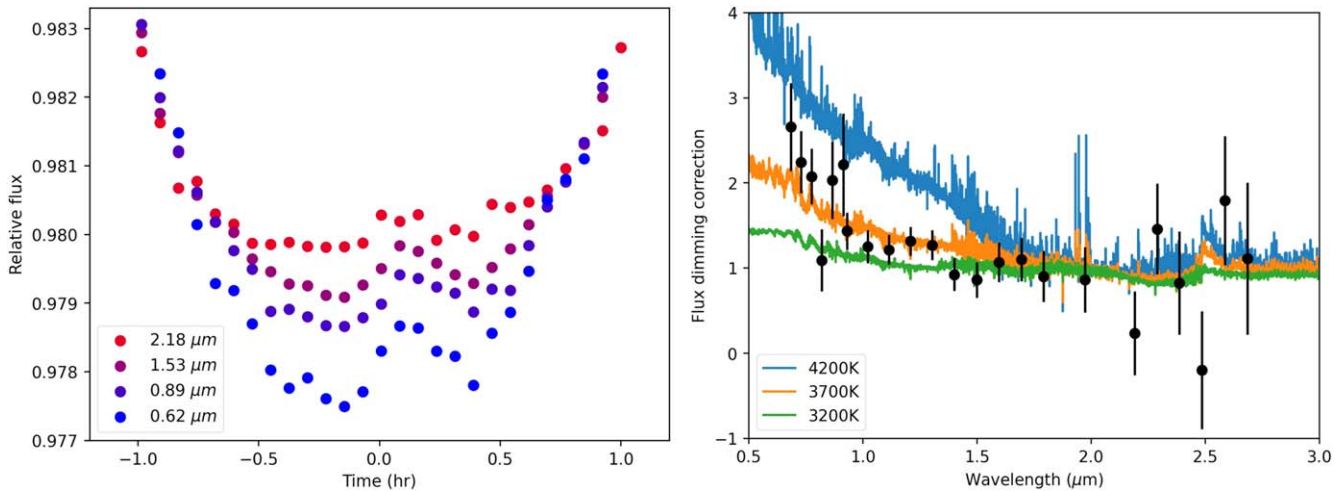
Figure 2. The transit light curve has a clear starspot crossing event starting around midtransit (left panel). The starspot crossing affects the light curve as a function of wavelength with shorter wavelengths being the most affected. We first measure the amplitude of the starspot at each wavelength and then use the PHOENIX stellar models to obtain a best-fit starspot temperature of 3596 ± 31 K (right panel). Assuming other unoccuated starspots are at a similar temperature, we then use the stellar flux variability level seen in TESS observations to estimate the dilution effect. We obtain a <20 ppm level dilution effect between 0.6 and 2.8 μm, which is much smaller than the uncertainties in the transmission spectrum.

to the stellar photosphere, we use the best-fit model from the white light fits and scale it for each wavelength (Sing et al. 2011).

The best-fit white light midtransit time (2459743.853395 ± 0.000023 MJD), semimajor axis ($a/R_{star} = 16.52 \pm 0.06$), and inclination (88.66 ± 0.03 degrees) are then fixed to fit the light curve from each column. There are four free parameters in the fit including the transit depth, a linear slope, a constant offset, and a scaling factor for the starspot crossing model. We used the `scipy.optimize.curvefit` function for individual wavelength channel fits. For the limb darkening, we used quadratic coefficients from the 3D stellar model in the Stagger grid (Magic et al. 2015). For the wavelength solution, we used the `jwst-niriss-wavemap-0021.fits` wavelength map file from the JWST calibration reference data system.

We compared our final reduced transmission spectrum to an independent reduction from Néstor Espinoza using the pipeline `TransitSpectroscopy`[10] and they are in excellent agreement as shown in the top panel of Figure 4.

2.3. Contamination and Dilution

To ensure the accuracy of our transmission spectrum we have investigated possible sources of contamination and dilution. We identify the following three sources that could potentially affect the planet spectrum.

2.3.1. Zeroth-order Contamination

As NIRISS/SOSS is a slitless spectrograph, nearby stars can overlap with the target's spectral trace. There are three clear zeroth-order nearby star contaminations in the observation as shown in the upper panel of Figure 1. Contamination 1 is on the second-order spectral trace but fortunately, it only affects the longer wavelength portion of the second order, which is not extracted due to the relatively low counts. It is also too far away from the first-order spectrum to cause dilution. Contamination 2 is more complex as it sits directly on the first-order dispersion and its brightness also varies in time (Figure 1). It is likely an

eclipsing binary with ingress starting ~2.4 hr after HAT-P-18b's midtransit; the observation only catches a partial egress but it has a V-shaped transit with a maximum dimming of ~12%. We masked this part of the spectrum (1.98–2.01 μm) in the analysis. Contamination 3 is located between the first and second order, but it has a long tail going across the second order around 0.7 μm. The tail leads to a wavelength-dependent dilution in the transit depth; therefore we removed the 0.68 to 0.72 μm part of the spectrum in the analysis.

2.3.2. A Nearby Source from Gaia

There is a nearby star (2″66 away) in the Gaia database (Gaia Collaboration et al. 2018; source ID: 1334573817793501696) that could cause dilution in the overlapped spectral dispersion. The companion has a delta magnitude of 4.587 and 4.898 fainter than HAT-P-18b, respectively, in the Gaia blue and red passbands. We performed a Gaia colors fit of the companion relative to HAT-P-18 ($T_{eff} = 4800 K$) and obtained a best-fit T_{eff} of 5500 K ± 300 K. Then we normalize the 5500 K and 4800 K PHOENIX models to the delta magnitude and calculate the dilution effect on the transit depth. Assuming the worst-case scenario of complete companion spectral overlap, the resulting dilution is less than 20 ppm between the 0.6 and 3 μm regions of the transit spectrum. This is much smaller than the uncertainties on the final transmission spectrum, and we only expect slight spectral overlap from the companion base depending on the position angle of the instrument. Therefore, we conclude it is safe to ignore this Gaia nearby source. We also checked archival infrared high-contrast imaging data and there are no other known nearby sources (Ngo et al. 2015, 2016).

2.3.3. Unoccuated Starspots

Unoccuated starspots can lead to a wavelength-dependent dilution effect on the transmission spectrum (Agol et al. 2010; Pont et al. 2013). To estimate the magnitude of this effect, we follow the steps detailed in Section 3.5 of Sing et al. (2011). We first fit for the starspot temperature using the best-fit starspot scaling factor at each wavelength. The best-fit starspot temperature is 3596 ± 31 K assuming a host star temperature of

---

[10] https://github.com/nespinoza/transitspectroscopy

4800 K (Figure 2). Next, we estimate the photometric stellar variability amplitude from TESS observations, which observed the star during sectors 25 and 26. After removing the transits in TESS, we used a Lomb–Scargle periodogram to find a best-fit variability period of $\sim$14.3 days, which is consistent with the reported stellar rotational period of 14.66 ± 0.03 days (Everett et al. 2013). The corresponding variability amplitude is 0.0724% and it is within the 0.1% level mean R-band brightness variation observed from the 12 month ground-based monitoring campaign (Kirk et al. 2017). Finally, we use Equations (4) and (5) from Sing et al. (2011) to calculate an expected dilution effect of <20 ppm between 0.6 and 3 μm in the transmission spectrum. Since this effect is much smaller than the uncertainties on the transmission spectrum, we conclude it is safe to ignore the unocculated starspots.

3. Detection of Excess Helium Absorption and Tail

We detect excess metastable 1083 nm helium absorption in the transmission spectrum. The helium line is not fully spectrally resolved with the SOSS ($R \sim 550$ at 1083 nm) but the transit depth from a 2 pixel wide bin (one resolution element) centered at 1083.065 and 1083.998 nm is visibly deeper than that in nearby pixels (Figure 3). We measure a helium transit depth of $1.97\% \pm 0.016\%$ with the 2 pixel bin relative to a nearby white light (40 pixel bin) depth of $1.88\% \pm 0.004\%$. This is consistent within 1σ to the $2.46\% \pm 0.15\%$ helium transit depth reported in Vissapragada et al. (2022) and Paragas et al. (2021) after accounting for the spectral resolution difference. Although our measurement is more diluted than that of Vissapragada et al. (2022), our detection of excess absorption is more statistically significant (5.6σ versus 4.3σ).

We also see evidence of a helium tail at egress (Figure 3). We subtracted the nearby white light from the helium light curve and the residual clearly shows asymmetry between ingress and egress. Future detailed follow-up 3D hydrodynamical simulations of the tail may tell us more about the escaping material and stellar environment of HAT-P-18b. A planetary tail from escaping helium has only previously been detected on WASP-107b (Allart et al. 2019; Kirk et al. 2020; Spake et al. 2021), WASP-69b (Nortmann et al. 2018), and HD 189733b (Guilluy et al. 2020). Previous ground-based observations of HAT-P-18b did not see the tail because the signal-to-noise of their excess absorption detection was lower than that of the detection we report here. This demonstrates the unmatched photometric precision from JWST compared to typical ground-based observatories. Although lower in spectral resolution compared to ground-based high-resolution spectrographs ($R > 10000$), JWST NIRSpec/G140H ($R \sim 2700$) is a promising instrument mode for helium observations thanks to its superior stability and precision.

3.1. Escaping Helium Modeling

We fit the metastable helium (Seager & Sasselov 2000) transmission spectrum between 1.07 and 1.10 μm with a 1D, isothermal Parker-wind model (Parker 1958) based on the p-winds code (version 1.3.0; Dos Santos et al. 2022) to determine the mass-loss rate of HAT-P-18b. This code applies the original formulation from Oklopčić & Hirata (2018) along with modeling improvements proposed in Lampón et al. (2021) and Vissapragada et al. (2022). We assume the planetary outflow has a He/H fraction of 10/90. We further assume that
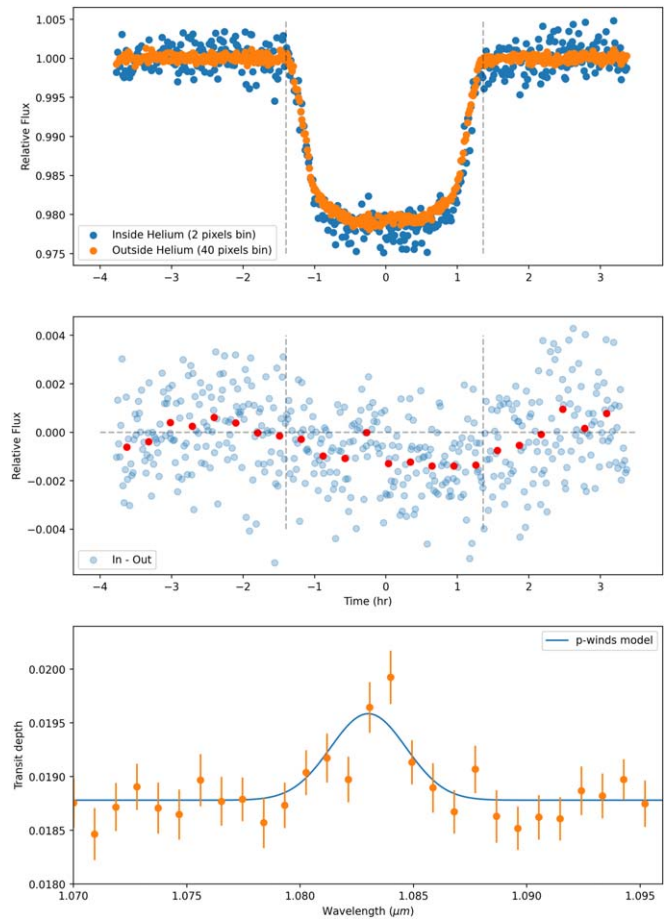

Figure 3. We detect escaping helium in HAT-P-18b. The top panel shows the light curve centered at the 1083 nm helium line vs. white light light curve from nearby pixels. The middle panel shows the residual (binned in red) from subtracting the outside helium light curve from the inside helium light curve. The residual clearly shows a deeper transit and a tail after the egress. The vertical gray dashed lines show the first and fourth contact and the horizontal gray dashed line is the zero residual level. The bottom panel is the transmission spectrum of HAT-P-18b at pixel level overplotted with the best-fit p-winds model.

the high-energy spectral energy distribution of HAT-P-18 is similar to HD 85512, and adopt the MUSCLES spectrum (Loyd et al. 2016; Youngblood et al. 2016) of the latter as a proxy when calculating the ionization balance in the planetary outflow. We took into account the Roche lobe effects and the fact that the planet is only irradiated over π steradians rather than the 4π steradians assumed by p-winds models.

Our forward models indicate that the mass-loss rate of 3.7×10^{10} g s^{-1} estimated by Vissapragada et al. (2022) for an outflow temperature of 8000 K is consistent with the observed JWST transmission spectrum in the metastable He feature (see Figure 3). Since the absorption profile is not resolved by NIRISS, there is a degeneracy between the escape rate and outflow temperature when fitting isothermal Parker-wind models to the data. Because of this degeneracy, solutions with lower mass-loss rates will fit the observation just as well if they have lower temperatures. This effect is also seen in the narrow-band photometry technique used by Vissapragada et al. (2022), and it is likely going to be a limitation in future NIRISS observations of He in other planets as well. High-resolution spectroscopy from the ground can resolve the planetary absorption and break this degeneracy.
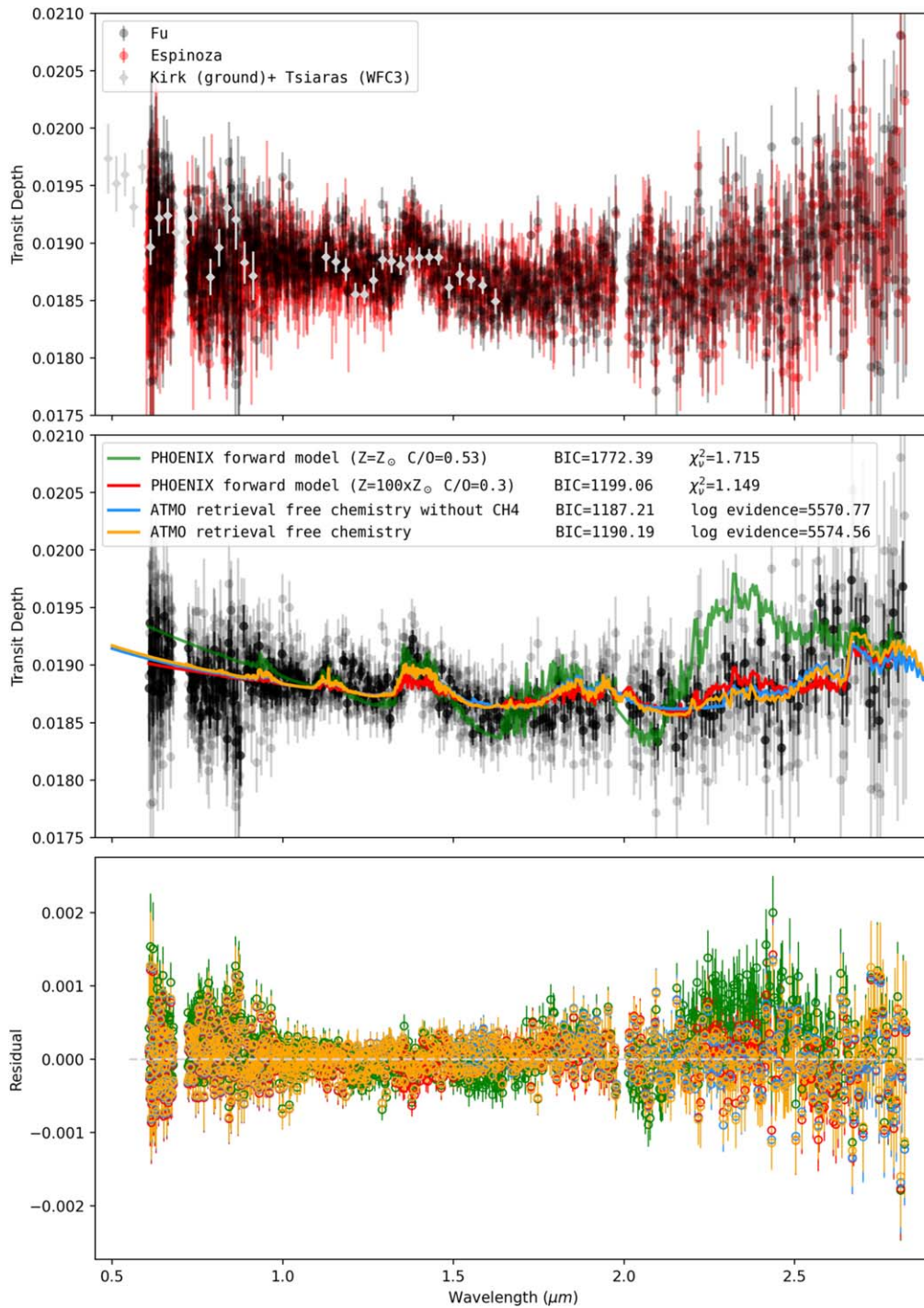
Figure 4. The top panel shows the comparison between two independent data reductions and previous observations from the ground (Kirk et al. 2017) and HST/WFC3 (Tsiaras et al. 2018) with no offsets applied. All data show excellent consistency with each other. The middle panel shows the spectrum (Fu version) overplotted with two PHOENIX forward models and two ATMO free chemistry retrieval best-fit models. The higher $R = 700$ spectrum is in gray and the lower $R = 200$ spectrum is in black. The retrieval is performed on the $R = 700$ spectrum. The lack of a clearly identifiable methane feature rules out the solar composition atmosphere. The 100 times solar metallicity and 0.3 C/O forward model provide a decent fit but underpredict the 1.4 μm water feature while overpredicting the 2.3 μm methane feature. The ATMO free chemistry retrieval (with H_2O, CO_2, CO, and CH_4) provides the best-fit model, and an identical retrieval without CH_4 gives a comparable fit. The log Bayesian evidence difference of 3.79 corresponds to moderate evidence supporting the detection of methane. The BIC metric slightly favors the retrieval without methane due to one less free fitting parameter. The bottom panel shows the corresponding residuals from the models in the middle panel. All models detect clear water absorption and a hazy atmosphere. The escaping helium part of the spectrum was excluded and modeled separately.

4. Atmospheric Retrievals and Modeling

4.1. PHOENIX Forward Model

PHOENIX is a self-consistent atmospheric forward model assuming local thermodynamic equilibrium and equilibrium chemistry (Lothringer et al. 2018). The transmission spectrum shows distinct haze (optical scattering slope), water, and the lack of strong methane features. Solar composition PHOENIX models fail to fit the spectrum as they largely overpredict the methane features (Figure 4). One way to suppress the methane
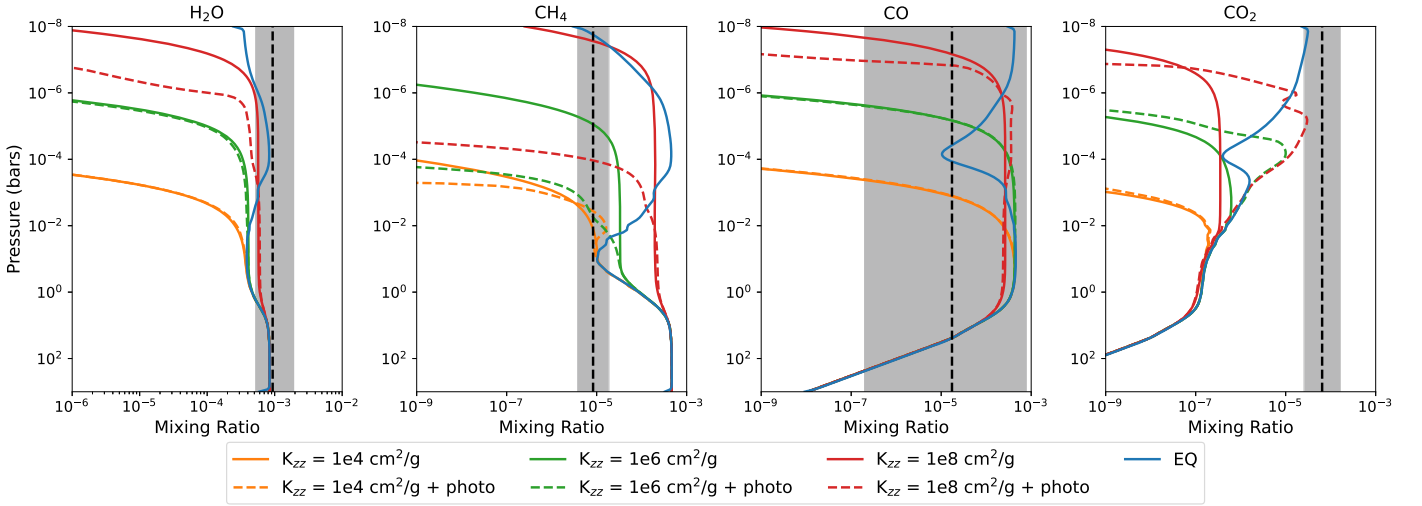
Figure 5. We explored the effects of vertical mixing and photochemistry using VULCAN (Tsai et al. 2021). The blue line is chemical abundance for H_2O, CH_4, CO, and CO_2 at each pressure level from the PHOENIX forward model assuming equilibrium chemistry and solar composition. The orange, green, and red lines show the abundance with different K_{zz} values. The dashed lines are with photochemistry turned on. The dashed black line and gray shaded regions are the retrieved constraints from ATMO. We see both vertical mixing and photochemistry are effective at removing methane from the atmosphere.

while preserving water is to increase the metallicity and decrease the C/O ratio. Therefore we generate a PHOENIX forward model grid at 10, 50, and 100 times solar metallicity and C/O ratios of 0.3 and 0.53 with various haze strengths and slopes. The best-fit PHOENIX model ($\chi^2_\nu = 1.149$ with 1013 degrees of freedom) has a 100 times solar metallicity and a 0.3 C/O ratio as shown (red) in the midpanel of Figure 4. It underpredicts the 1.4 μm water feature while overpredicting the 2.3 μm methane feature. This suggests that the equilibrium chemistry model struggles to effectively remove methane without also oversuppressing the water features.

We further explored methane depletion by running models with molecular abundances quenched at 0.1, 1 bar to simulate the effects of vertical mixing. The methane abundance at 0.1 bar is a few orders of magnitude below its maximum abundance, resulting in the most methane depletion if quenching occurs near this level in the atmosphere (Figure 5). We then pick the 0.1 bar as the quench point and were able to reduce the best-fit forward model metallicity from 100 to 50 times solar. The 0.1 bar pressure level was selected solely based on examining the methane abundance profile and finding the corresponding pressure level for the minimum methane mixing ratio. Only CH_4, CO_2, CO, and H_2O were quenched in our model and quenching approximation does not work for every chemical species (Tsai et al. 2017).

We also tested the effects of photochemistry and vertical mixing using the chemical kinetics code VULCAN (Tsai et al. 2021). We ran VULCAN using the atmosphere structure from the best-fit PHOENIX model with default parameters using the HCNO chemical network with various vertically-constant K_{zz} both with and without photochemistry. Abundance profiles of H_2O, CH_4, CO, and CO_2 are shown in Figure 5. Various scenarios with vertical mixing and photochemistry can lead to significant methane depletion, matching constraints from the retrieval, but determining the specific contribution from each effect at work in HAT-P-18b requires a more detailed retrieval analysis, which is beyond of the scope of this Letter.

4.2. ATMO Free Chemistry Retrieval

To better explore the abundance and significance of the detected chemical species, we also ran a free chemistry retrieval with ATMO (Tremblin et al. 2015, 2016) including temperature, radius, cloud deck pressure, haze strength, haze scattering slope, H_2O, CO_2, CO, and CH_4. We detected water with a volume mixing ratio (VMR) of $\log(H_2O) = -3.03^{+0.31}_{-0.25}$ and retrieved a methane abundance of $\log(CH_4) = -5.08^{+0.35}_{-0.34}$. Compared to the PHOENIX forward model, the water abundance is consistent with a $\sim$5 times solar metallicity atmosphere at 1 mbar assuming chemical equilibrium and a solar C/O ratio while methane is about 2 orders of magnitude lower. We find a CO abundance of $\log(CO = -4.76^{+1.65}_{-1.94})$ and a CO_2 abundance of $\log(CO_2 = -4.19^{+0.4}_{-0.4})$ are more weakly constrained due to the lack of spectral features at these wavelengths, but their low retrieved abundances are consistent with the forward model predictions since most of the carbon should be in the form of methane.

To further investigate the presence of methane in the atmosphere we ran another identical retrieval but without CH_4. The best-fit retrieval model (Bayesian information criterion, BIC = 1190.19 and log Bayesian evidence = 5570.77) produced a comparable fit to the first full retrieval (BIC=1187.21 and log Bayesian evidence = 5574.56) with methane included. The difference of 3.79 in log Bayesian evidence would correspond to moderate evidence (Trotta 2008) supporting the detection of methane. However, the BIC favors the retrieval without methane due to one less free fitting parameter. The retrieved VMR of water $(H_2O) = -3.8^{+0.17}_{-0.17}$ stays unchanged and CO_2 $(\log(CO_2) = -5.72^{+0.61}_{-0.72})$ remains unconstrained, but the CO $(\log(CO) = -3.38^{+0.61}_{-1.02})$ abundance increases. We believe this is due to the overlapping feature from CH_4 and CO around 2.3 μm. Based on the free chemistry retrieval results, we are hesitant to conclude clear detection of methane in the atmosphere of HAT-P-18b. A definitive detection and more stringent limits on CH_4, CO, and CO_2 could be made with NIRSpec G395H, as the molecular signatures of all three

Table 1
HAT-P-18b Transmission Spectrum

Wavelength Midpoint (μm)	Transit Depth (ppm)	Uncertainty (ppm)
0.6078	18908	1009
0.6087	18903	616
0.6096	19277	598
0.6104	19544	653
0.6113	19468	525

(This table is available in its entirety in machine-readable form.)

carbon-bearing species are considerably stronger at longer wavelengths.

5. Discussion and Conclusion

The lack of identifiable methane features in the transmission spectrum (Table 1) challenges the simple equilibrium chemistry assumption and motivates the exploration of additional physical processes such as vertical mixing and photochemistry (Cooper & Showman 2006; Steinrueck et al. 2019; Drummond et al. 2020). Vertical mixing brings up material from deeper in the planet and changes the atmospheric composition probed by the transmission spectrum (Zahnle & Marley 2014; Fortney et al. 2020). Depending on the planet's thermal structure and horizontal circulation, mixing could lead to the destruction of methane from the hotter interior or dayside of the planet (Komacek et al. 2019). On the other hand, photochemistry at the top of the atmosphere can break down methane into other hydrocarbon and haze precursors (Tsai et al. 2021). The detection of a strong haze layer on HAT-P-18b is consistent with the presence of a methane-derived photochemical haze.

We present the NIRISS/SOSS transmission spectrum of HAT-P-18b, an inflated Saturn-like mass planet with an equilibrium temperature of ∼850 K. The 0.6 to 2.8 μm wavelength coverage from SOSS gives us the first look at this planet in the infrared. We detect water, an escaping helium tail, and methane depletion in the hazy atmosphere of HAT-P-18b. The water and helium spectral features are consistent with previous observations (Tsiaras et al. 2018; Paragas et al. 2021; Vissapragada et al. 2022). The detection of a helium tail showcases the unparalleled level of photometric precision from JWST compared to ground-based observation. JWST NIRSpec/G140H ($R \sim 2700$) will be the ideal instrument mode for any future study of escaped helium.

The methane-depleted atmosphere adds to the growing observational evidence (Stevenson et al. 2010; Benneke et al. 2019; Kreidberg et al. 2019) of missing methane in sub-1000 K planets. This calls for including disequilibrium chemistry processes such as vertical mixing and photochemistry, which are effective at delaying the onset of detectable methane features to lower equilibrium temperatures. The fast-growing JWST data sets of exoplanet atmospheres will certainly challenge our simple model assumptions and additional modeling efforts with more physical processes will be needed.

Future follow-up observation of HAT-P-18b with JWST NIRSpec/prism covering the 2.8 to 5.3 μm wavelength range will be useful at determining how depleted methane is in the atmosphere by measuring the stronger 3 to 4 μm methane

feature. Additionally, it will better constrain the planet's C/O ratio by simultaneous coverage of CO and CO_2 features at 4 and 5 μm.

ORCID iDs

Guangwei Fu ● https://orcid.org/0000-0002-3263-2251
Néstor Espinoza ● https://orcid.org/0000-0001-9513-1449
David K. Sing ● https://orcid.org/0000-0001-6050-7645
Joshua D. Lothringer ● https://orcid.org/0000-0003-3667-8633
Leonardo A. Dos Santos ● https://orcid.org/0000-0002-2248-3838
Zafar Rustamkulov ● https://orcid.org/0000-0003-4408-0463
Drake Deming ● https://orcid.org/0000-0001-5727-4094
Eliza M.-R. Kempton ● https://orcid.org/0000-0002-1337-9051
Thaddeus D. Komacek ● https://orcid.org/0000-0002-9258-5311
Heather A. Knutson ● https://orcid.org/0000-0002-5375-4725
Loïc Albert ● https://orcid.org/0000-0003-0475-9375
Klaus Pontoppidan ● https://orcid.org/0000-0001-7552-1562
Joseph Filippazzo ● https://orcid.org/0000-0002-0201-8306

References

Agol, E., Cowan, N. B., Knutson, H. A., et al. 2010, ApJ, 721, 1861
Allart, R., Bourrier, V., Lovis, C., et al. 2019, A&A, 623, A58
Benneke, B., Knutson, H. A., Lothringer, J., et al. 2019, NatAs, 3, 813
Cooper, C. S., & Showman, A. P. 2006, ApJ, 649, 1048
Dos Santos, L. A., Vidotto, A. A., Vissapragada, S., et al. 2022, A&A, 659, A62
Drummond, B., Hébrard, E., Mayne, N. J., et al. 2020, A&A, 636, A68
Everett, M. E., Howell, S. B., Silva, D. R., & Szkody, P. 2013, ApJ, 771, 107
Foreman-Mackey, D., Hogg, D. W., Lang, D., & Goodman, J. 2013, PASP, 125, 306
Fortney, J. J., Visscher, C., Marley, M. S., et al. 2020, AJ, 160, 288
Gaia Collaboration, Brown, A. G. A., Vallenari, A., et al. 2018, A&A, 616, A1
Guilluy, G., Andretta, V., Borsa, F., et al. 2020, A&A, 639, A49
Hartman, J. D., Bakos, G. A., Béky, B., et al. 2012, AJ, 144, 139
Kasting, J. F., Zahnle, K. J., & Walker, J. C. G. 1983, PreR, 20, 121
Kirk, J., Alam, M. K., López-Morales, M., & Zeng, L. 2020, AJ, 159, 115
Kirk, J., Wheatley, P. J., Louden, T., et al. 2017, MNRAS, 468, 3907
Komacek, T. D., Showman, A. P., & Parmentier, V. 2019, ApJ, 881, 152
Kreidberg, L. 2015, PASP, 127, 1161
Kreidberg, L., Koll, D. D. B., Morley, C., et al. 2019, Natur, 573, 87
Lampón, M., López-Puertas, M., Sanz-Forcada, J., et al. 2021, A&A, 647, A129
Lothringer, J. D., Barman, T., & Koskinen, T. 2018, ApJ, 866, 27
Loyd, R. O. P., France, K., Youngblood, A., et al. 2016, ApJ, 824, 102
Magic, Z., Chiavassa, A., Collet, R., & Asplund, M. 2015, A&A, 573, A90
Miller-Ricci Kempton, E., Zahnle, K., & Fortney, J. J. 2012, ApJ, 745, 3
Moses, J. I., Visscher, C., Fortney, J. J., et al. 2011, ApJ, 737, 15
Ngo, H., Knutson, H. A., Hinkley, S., et al. 2015, ApJ, 800, 138
Ngo, H., Knutson, H. A., Hinkley, S., et al. 2016, ApJ, 827, 8
Nortmann, L., Pallé, E., Salz, M., et al. 2018, Sci, 362, 1388
Oklopčić, A., & Hirata, C. M. 2018, ApJ, 855, L11
Paragas, K., Vissapragada, S., Knutson, H. A., et al. 2021, ApJL, 909, L10
Parker, E. N. 1958, ApJ, 128, 664
Pont, F., Sing, D. K., Gibson, N. P., et al. 2013, MNRAS, 432, 2917
Pontoppidan, K., Blome, C., Braun, H., et al. 2022, ApJL, 936, L14
Seager, S., & Sasselov, D. D. 2000, ApJ, 537, 916
Sing, D. K., Pont, F., Aigrain, S., et al. 2011, MNRAS, 416, 1443
Spake, J. J., Oklopcic, A., & Hillenbrand, L. A. 2021, AJ, 162, 284
Steinrueck, M. E., Parmentier, V., Showman, A. P., Lothringer, J. D., & Lupu, R. E. 2019, ApJ, 880, 14
Stevenson, K. B., Harrington, J., Nymeyer, S., et al. 2010, Natur, 464, 1161
The JWST Transiting Exoplanet Community Early Release Science Team, Ahrer, E.-M., Alderson, L., et al. 2022, Natur, in press

Thompson, M. A., Krissansen-Totton, J., Wogan, N., Telus, M., & Fortney, J. J. 2022, PNAS, 119, e2117933119
Tremblin, P., Amundsen, D. S., Chabrier, G., et al. 2016, ApJ, 817, L19
Tremblin, P., Amundsen, D. S., Mourier, P., et al. 2015, ApJ, 804, L17
Trotta, R. 2008, ConPh, 49, 71
Tsai, S.-M., Lyons, J. R., Grosheintz, L., et al. 2017, ApJS, 228, 20
Tsai, S.-M., Malik, M., Kitzmann, D., et al. 2021, ApJ, 923, 264
Tsiaras, A., Waldmann, I. P., Zingales, T., et al. 2018, AJ, 155, 156
Vissapragada, S., Knutson, H. A., Greklek-McKeon, M., et al. 2022, arXiv:2204.11865
Youngblood, A., France, K., Loyd, R. O. P., et al. 2016, ApJ, 824, 101
Zahnle, K. J., & Marley, M. S. 2014, ApJ, 19, 41